Electronic Supporting Information

Assembled mechanical metamaterials with integrated functionalities of programmable multistability and multitransition behaviors

Jian He, Yaohui Wang, Zhengquan Shen, Liang Xia, Yi Xiong**

J. He, Y. Wang, Y. Xiong

School of System Design and Intelligent Manufacturing, Southern University of Science and Technology, Shenzhen 518055, China.

E-mail: xiongy3@sustech.edu.cn

Z. Shen

Dyson School of Design Engineering, Imperial College London, Exhibition Road, London. SW7 2DB, UK.

L. Xia

State Key Laboratory of Intelligent Manufacturing Equipment and Technology, Huazhong University of Science and Technology, Wuhan, 430074, China.
E-mail: xialiang@hust.edu.cn

In this supplementary document, we provide Sections S1 to S13.

Other supplementary materials for this manuscript include Videos S1 to S8.

S1. Parametrization and underlying bistable mechanism of the curved beam

The proposed shape-describing function $y(x) = -H/2 \cos((x/W)^g \pi)$, $x \in [0, W]$ is capable of describing variant beam shapes by tuning the shape coefficient g, as the curves in Fig. S1a for g = 1.2, 1.5, 2 ($\geq$ 1), respectively. Moreover, a second series of beam shapes is gained by introducing the operator $\mathscr{R}$:g, which indicates that the beam shape of the value g can be reckoned as a symmetric reflection of the beam shape of the same value g along both the X-axis and Y-axis. Fig. S1b shows the snapping force F_{max} and the trough force F_{min} of the proposed parameterized beams during loading evaluated by numerical simulation. The beams with g and $\mathscr{R}$:g ranging from 1 to 2 exhibit a transition from bistability to monostability. Compared to the force-displacement curve of Beam 1 with g = 1[1,2], the force-displacement curve of Beam 2 with g = 2 possesses a smaller value of F_{max} and a positive value of F_{min} with an overall smoother loading trend. Notably, the beam's geometry is determined by varying values of g and further changes the stiffness distribution of beams (Fig. S2). When the stiffness of the loading end is smaller than the stiffness of the fixed end, e.g., g = 1, the beam near the loading end deforms first (strain = 0.1), thus forming a wave peak pattern; while when the stiffness of the loading end is larger than the stiffness of the fixed end, e.g., g = 2, the beam at the fixed end deforms first, thus forming a wave trough pattern. It is noted that the beams with $g \geq 1.2$ all exhibit a wave trough pattern during loading, which can be utilized to achieve multi-stage state transition behaviors by incorporating contact block (CB) units beneath the beam as contact constraints. Here, we choose Beam 2 for the remaining investigation.

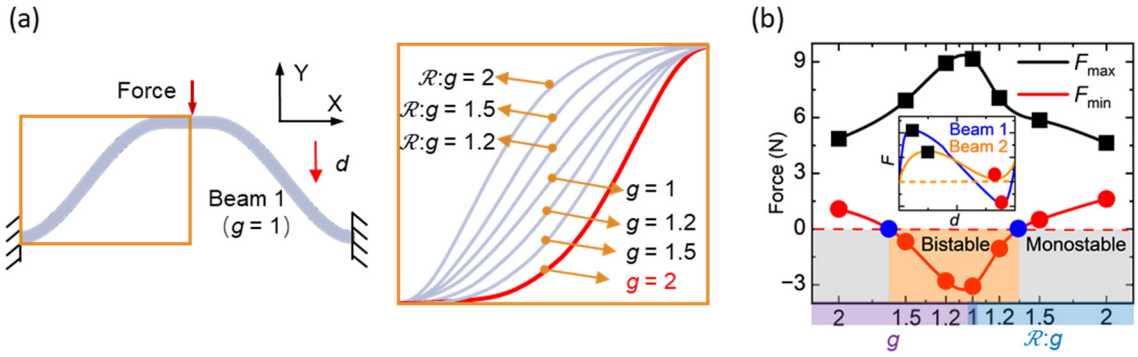

Fig. S1. The parameterized curved beams. (a) The variant beam shapes by tuning the shape coefficient g and the operator $\mathscr{R}$:g. (b) The snapping force F_{max} and the trough force F_{min} of beams with different coefficients g during loading evaluated by numerical simulation. The trough force $F_{min} < 0$ indicates that the beam is bistable.

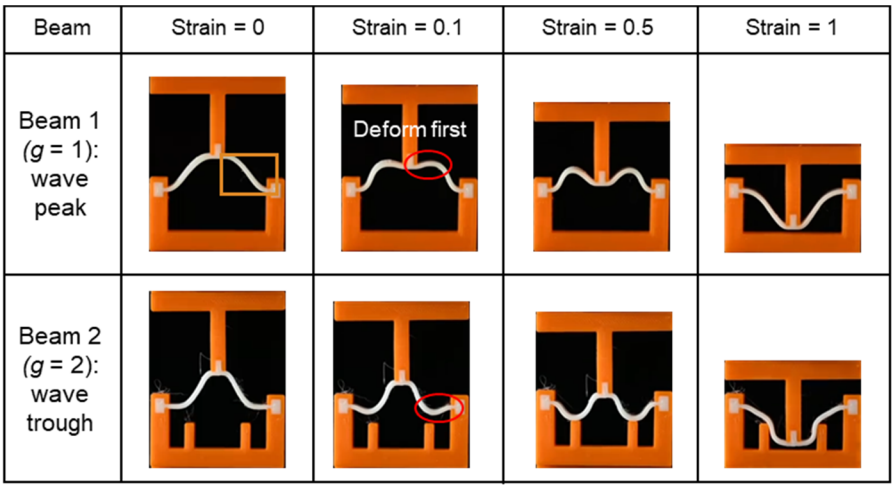

Fig. S2. The comparison of beams with varying parameter g

The unit cell with Beam 2 changes from monostability to bistability through the introduced contact constraints. Inspired by badminton storage, without any constraints, a badminton shuttlecock drops from the bucket due to gravity (Fig. S3a). The bucket, with a narrowed opening, functions as a clamp that alters the local deformation of the shuttlecock and secures it in place (Fig. S3b). We utilize the double trough deformation pattern of Beam 2 and through the introduction of CB units, the unit cell transitions into the other stable state.

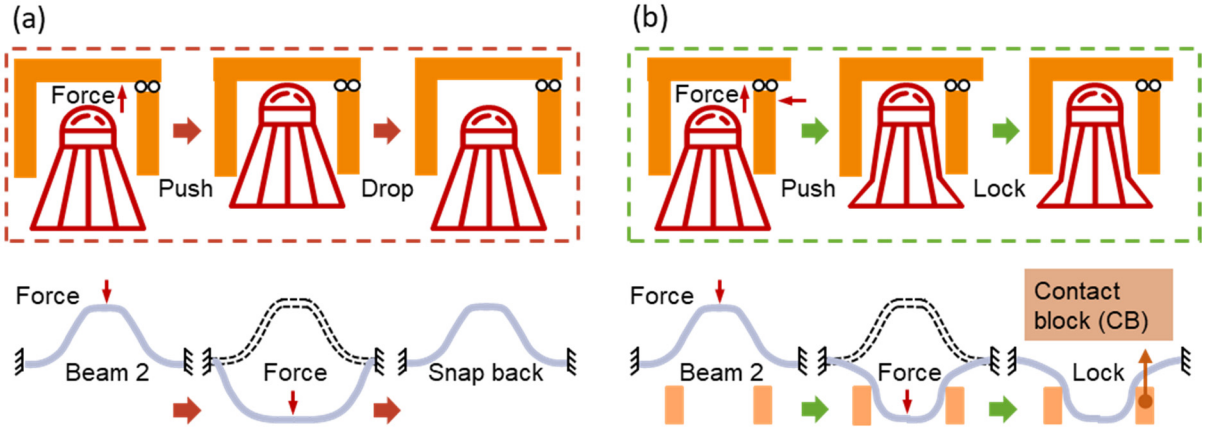

Fig. S3. The bistable mechanism of the assembled unit cell. (a) Monostability of the unit cell without CB. (b) Bistability of the unit cell with CB.

S2. FDM manufacturing details and material property

The samples were printed using an Ultimaker S5 3D printer (Ultimaker B.V., Utrecht, The Netherlands), adopting a dual material extrusion method layer by layer (Fig. S4a). PLA (Polymaker, China) was extruded through Nozzle 1, while TPU (Polymaker, China) was extruded through Nozzle 2. The TPU material has a density of ρ = 1230 kg/m^3, a tensile strength

of 23.9 MPa, and exhibits typical elastic properties with Young's modulus E = 11.7 MPa and Poisson's ratio υ = 0.46. The diameter of the nozzles is 0.4 mm and the layer height is 0.1 mm in the Z direction. After adjusting the printing parameters, such as flow, line width, and print speed, the resolution of the printer in X/Y plane is empirically estimated to be 0.2 mm. PLA parts connecting the two ends of the TPU beam serve as a fixed structure. PLA parts above the TPU beam act as a force-transmitting structure during a uniaxial cyclic test (ZwickiLine Z0.5 to Z5.0, ZwickRoell Pre. Ltd., Australia). The size of the unit cell is 47 mm × 60 mm with an out-of-plane thickness of 8 mm and more sizes of the PLA structure are shown in Fig. S4b.

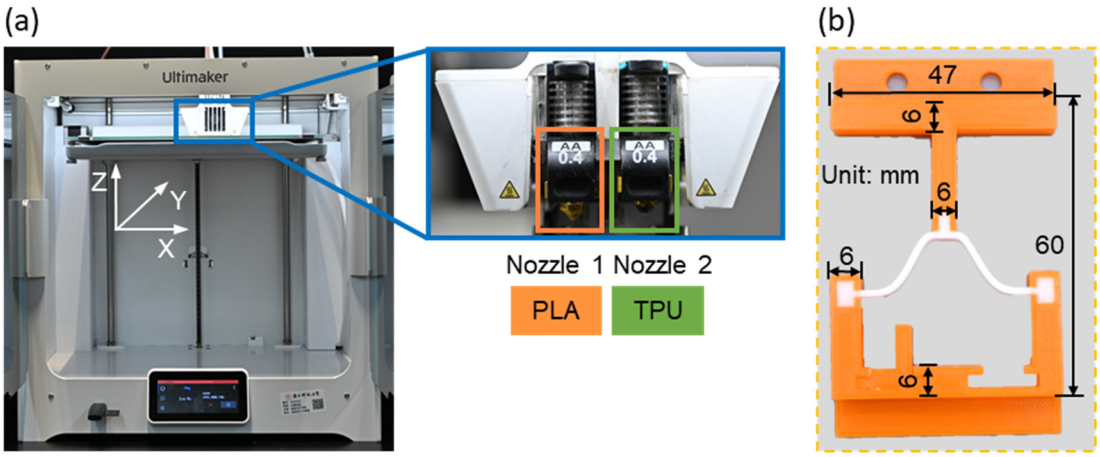

Fig. S4. (a) 3D printer for printing samples. (b) Geometrical details of printed samples.

The material properties of the TPU were further experimentally characterized and utilized as inputs for numerical simulation. A strip (1.3 mm × 8 mm × 30 mm) was printed and tested under a uniaxial tensile test at a loading rate of 0.1 mm/s. The tensile results indicate a nonlinear stress-strain relationship under large deformation (Fig. S5a) and a Mooney-Rivlin model is used to describe the TPU stress-strain behavior and the form of strain energy density E with two parameters is applied[3]:

$$E = C_{10}(\overline{I_1}\text{-}1)+C_{01}(\overline{I_2}\text{-}1)+\frac{1}{D_1}(J\text{-}1)^2, \quad \text{(S1)}$$

where $\overline{I_1}$ and $\overline{I_2}$ are the first and second deviatoric strain invariants; J is the determinant of the deformation gradient tensor; C_{10} and C_{01} are material parameters obtained by fitting the experimental strain-stress curve; D_1 is the temperature dependent material parameter. As the parameters C_{10} = -0.54516, C_{01} = 6.04727, D_1 = 0.001, the fitted stress-strain curve matches the experimental data well. Additionally, Young's modulus of the used TPU is measured at 5.7 MPa.

A uniaxial cyclic test was conducted on the unit cell with Beam 1. As shown in Fig. S5b, the unit cell exhibits a larger loading force during the initial loading stage. This can be mainly

attributed to two reasons: material initialization and viscoelasticity of TPU materials[4]. Firstly, the TPU material is in its pristine state, requiring significant energy to overcome initial resistance to deformation as the internal molecular chains, segments, and microstructural components rearrange to accommodate the applied load. This change can not recover rapidly, leading to lower stiffness and load-carrying capacity in subsequent cycle tests. Secondly, the viscoelasticity of TPU material exhibits stress relaxation, where stress decreases over time under constant strain. During the first loading, high initial stress is generated, but over time, this stress relaxes due to internal molecular motions that dissipate energy. As the material undergoes subsequent loading cycles, the already relaxed state means less force is required to achieve the same deformation. Subsequent stages of cyclic testing reveal consistent stress-strain curves during loading and unloading processes. In this study, we focus on the performance of the structure under the first loading and unloading phases.

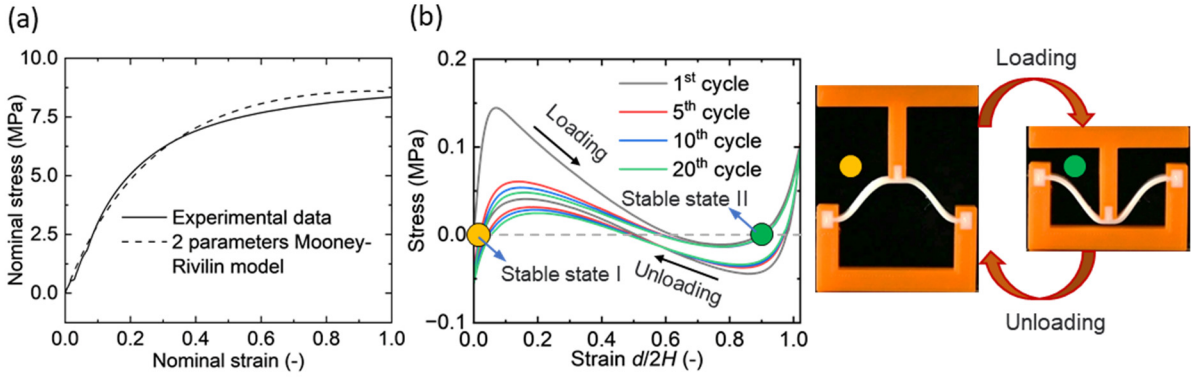

Fig. S5. (a) Experimental and fitting stress-strain curve comparison for the TPU strip. (b) The stress-strain curve and stable states for Beam 1 under a uniaxial cyclic test.

S3. Numerical simulation of the 2D unit cell and the region of interest for CB

In this work, commercial finite element software ABAQUS was used to model and simulate the deformation process of the designed structure. The deformation process is considered quasi-static due to the low loading rate, and thus viscoelastic behavior is disregarded. The geometry nonlinearity effect is enabled and an automatic stabilization by a dissipated energy fraction of 0.0001 and a maximum ratio of 0.01 to strain energy is used to stabilize the solver. The boundary condition of the unit cell is depicted in Fig. S6a. The PLA material is modeled as a high-modulus isotropic material 'rigid'. The lower part of the PLA material is set as encastred, while a displacement load of 24 mm is applied to the upper part of the PLA material. The interfaces between TPU and PLA are set as a rigid body constraint, which results in the TPU beam being fixed at both ends and loaded at the top. Since the TPU beam makes contact with

CB during the deformation process, surface-to-surface self-contacts based on the penalty method are defined by assuming the friction coefficient as 0.6[5]. The C3D8RH element which is a hybrid formulation element is assigned to the TPU beam to keep consistent with the incompressible material model while the C3D8R element is assigned to all other parts (PLA). The discretized mesh model is shown in Fig. S6b, and the beam body and CB part where the contact probably exists are locally refined to ensure the simulation accuracy and convergence.

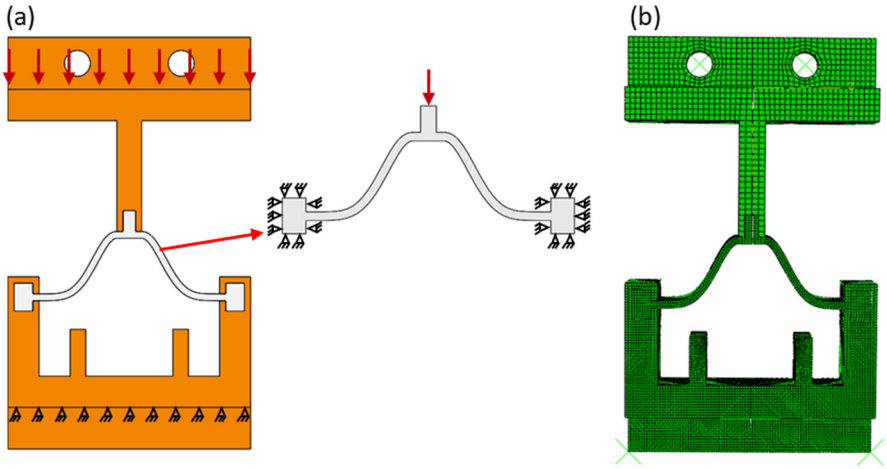

Fig. S6. (a) The boundary condition and (b) the discretized mesh model of the 2D unit cell.

We determined the region of interest for CB to efficiently explore the CB effect on the state transition behavior of the assembled unit cell. Since the point at the bottom of the beam initially contacts CB, we got a series of bottom points of the beam through numerical simulation in Fig. S7. During the entire deformation process, the bottom points of the beam exhibit space concentration as strain ($d/2H$) varies from 0.13 to 0.79. Consequently, we identified the area highlighted by a red box as the region of interest for CB, wherein CB spans a range of w/W from 0.33 to 0.67 and h/H from 0.13 to 0.79. Beyond this region, at small w and small h, CB has a limited effect on the transition behavior. Conversely, at large w and small h, where CB is close to the loading end, the beam is more susceptible to damage. Additionally, the regularity of transition behavior outside the region of interest for CB is compromised.

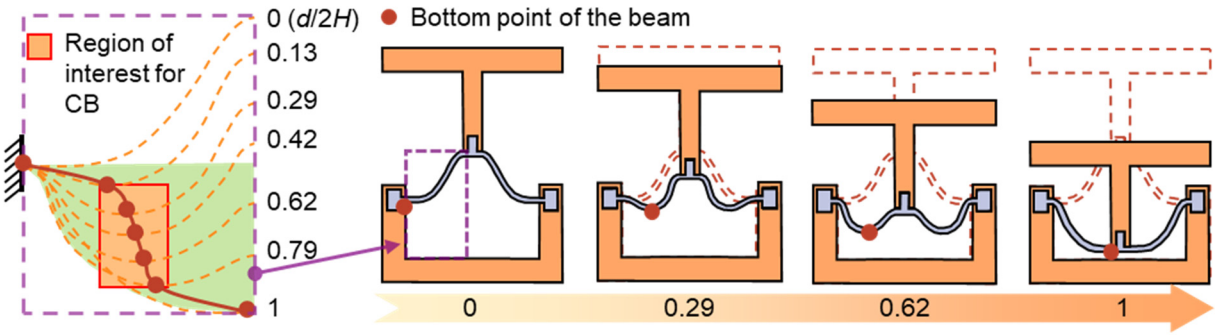

Fig. S7. Region of interest for CB determined by the bottom point of the beam during loading.

S4. Analysis of the slip phenomenon

As mentioned in the paper, the assembled unit cell shows a steep increase in the force value with an increment of displacement during the 2nd-stage deformation. It is worth noting that the beam slips at some CB positions during loading (Fig. S8a), reflecting as a force rebound on the transition behavior. After contacting CB, the beam first slides on the CB platform (2nd-stage-i) and then relies on the contact fulcrum to rotate and stretch (2nd-stage-ii). A distinct area marked by a red ellipse can be observed on the stress-strain curve. The slip phenomenon prevents the local excessive deformation of the beam while maintaining the level of stress values. Thus, the energy absorption of the unit cell is improved.

To better understand the mechanism of the slip behavior, when Beam 2 makes contact with CB, we classify the cases into three based on the relative position of the contact point between Beam 2 and CB and the bottom point of Beam 2 (Fig. S8b). In Case 1, exemplified by CB positioned at 0.33_0.13, the contact point lies to the left of the bottom point of Beam 2, leading to a scenario where no slip occurs. In Case 2, the contact point coincides with the bottom point of Beam 2. In this case, a coefficient f_s is introduced to explain whether a slip occurs. The dashed red lines (assuming a rigid rod) connect the contact point and the loading end, simplifying the force transmission path of the beam in the 2nd-stage deformation. The inclination γ governs the magnitude of the force components (the shear force F_h, the vertical force F_v) at the point of contact. Force analysis of the contact point on CB, we get:

$$\begin{aligned} F_v &= F_{rod}\sin(\gamma), \\ F_h &= F_{rod}\cos(\gamma), \end{aligned} \tag{S2}$$

where F_{rod} is the force transmitted by the rigid rod:

$$F_{rod} = F_{load}\sin(\gamma). \tag{S3}$$

Considering the friction coefficient μ on the contact surface, the coefficient f_s is defined as:

$$f_s = \frac{\mu F_v}{F_h} = \mu \tan(\gamma). \quad \text{(S4)}$$

When the coefficient $f_s < 1$, the slip phenomenon occurs, exemplified by the CB position at 0.6_0.63. Case 3 (the contact point is to the right of the bottom point of Beam 2) is similar to Case 2, where the contact point is on the upper left point of CB. Due to a small γ, the slip phenomenon commonly occurs in this case. However, since CB is close to the loading end, Case 3 tends to cause beam damage during mechanical tests, which falls outside the region of interest for CB in the subsequent study.

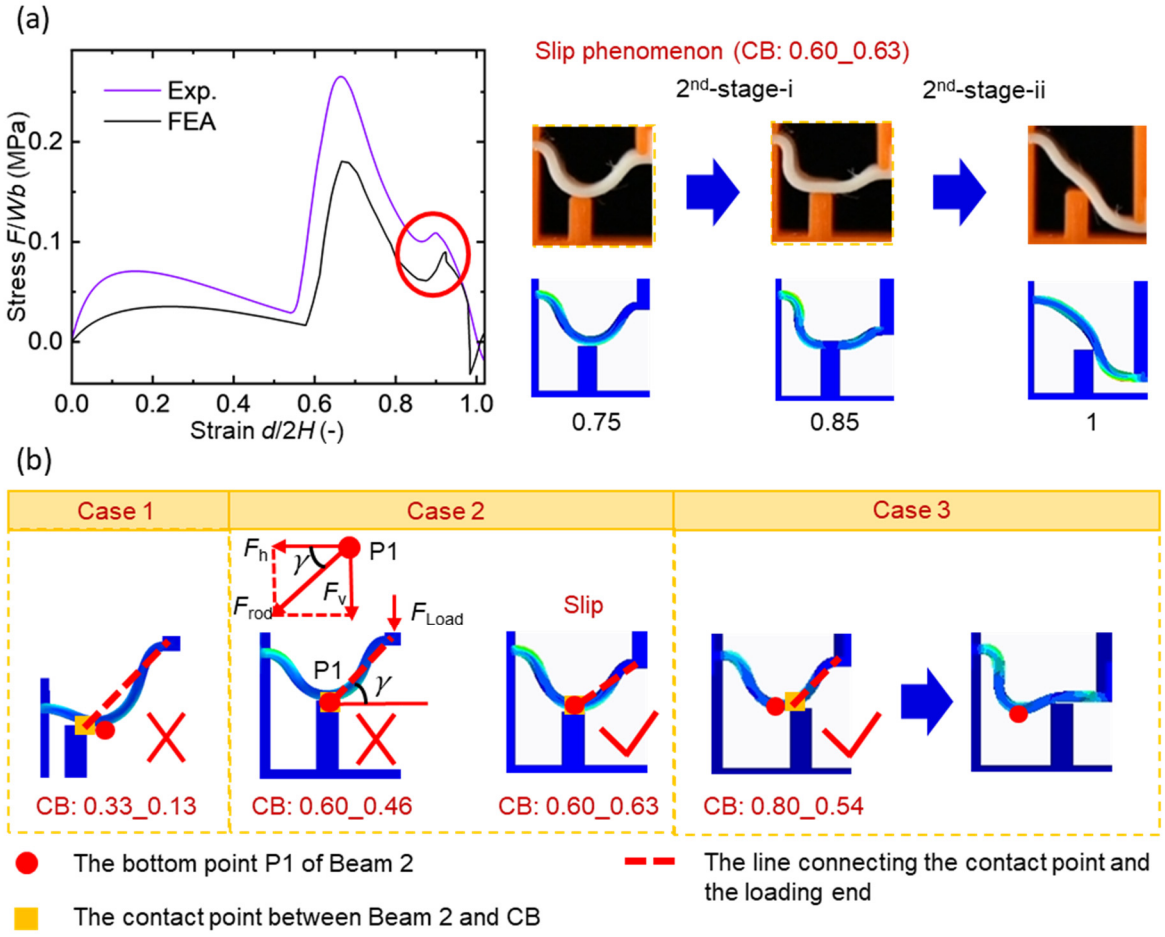

Fig. S8. Analysis of the slip phenomenon. (a) Experiment and numerical simulation of the unit cell with slip phenomenon. (b) Three cases classified by the relative position of the contact point between Beam 2 and CB and the bottom point of Beam 2, when Beam 2 makes contact with CB.

S5. Spring model for Single-CB design

As shown in Fig. S9, the deformation of the unit cell during a uniaxial cyclic test is represented by the compressive (K_s) and torsional (K_r) springs[6]. During loading, the

deformation process of the beam can be divided into two stages. Before Beam 2 makes contact with CB, the switch S_1 is off while the switch S_2 is on, the compressive spring K_{s1} and the torsional spring K_{r1} transfer loads, reckoned as the 1st-stage deformation. When Beam 2 makes contact with CB, the switches S_1, S_2 both reverse their states, thus K_{s2} and K_{r2} are activated to transfer loads, reckoned as the 2nd-stage deformation. The geometrical parameters W_1 (W_2), H_1 (H_2) are the equivalent width and height of the 1st-stage (2nd-stage) deformation respectively.

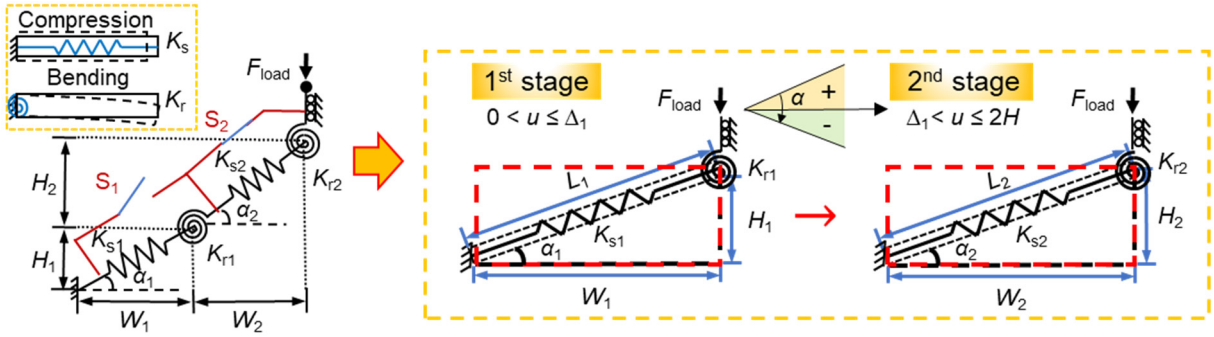

Fig. S9. The two stages of the proposed Single-CB spring model.

The total potential energy E_s of the whole system consists of the elastic strain energy (the stretching energy indicated by compression of K_s and the bending energy indicated by the rotation of K_r and the energy caused by the external force). Depending on whether the beam is in contact with the CB or not, E_s is a piecewise function, expressed as:

$$E_s = \begin{cases} K_{s1}\left[\sqrt{H_1^2+W_1^2}-\sqrt{(H_1-u)^2+W_1^2}\right]^2+K_{r1}\left[\alpha_1-\arctan\left(\frac{H_1-u}{W_1}\right)\right]^2 & 0<u\le\Delta_1 \\ -F_{load}u, & \\ K_{s1}\left[\sqrt{H_1^2+W_1^2}-\sqrt{(H_1-\Delta_1)^2+W_1^2}\right]^2+K_{r1}\left[\alpha_1-\arctan\left(\frac{H_1-\Delta_1}{W_1}\right)\right]^2 & \\ +K_{s2}\left[\sqrt{H_2^2+W_2^2}-\sqrt{\left(H_2-(u-\Delta_1+\delta)\right)^2+W_2^2}\right]^2 & \Delta_1<u\le 2H \\ +K_{r2}\left[\alpha_2-\arctan\left(\frac{H_2-(u-\Delta_1+\delta)}{W_2}\right)\right]^2+T_{crs}-F_{load}u. & \end{cases} \tag{S5}$$

Beam 2 undergoes the 1st-stage deformation when $0<u\le\Delta_1$, and within the range $\Delta_1<u\le 2H$, Beam 2 is in the 2nd-stage deformation after contacting CB, where the total displacement process of the beam is constant $2H$ = 24 mm. The term T_{crs} is added to numerically supplement the energy of the slip condition. By utilizing the stationary condition of the total potential energy[7]:

$$\frac{\partial E_{\mathrm{s}}}{\partial u}=0. \tag{S6}$$

The force (F_{load})-displacement (u) relationship can be obtained:

$$F_{\mathrm{load}}=\begin{cases} 2K_{\mathrm{s1}}\left[\sqrt{{H_1}^2+{W_1}^2}-\sqrt{(H_1-u)^2+{W_1}^2}\right]\dfrac{(H_1-u)}{\sqrt{(H_1-u)^2+{W_1}^2}} & \\ +2W_1K_{\mathrm{r1}}\dfrac{\left[\alpha_1-\arctan\left(\dfrac{H_1-u}{W_1}\right)\right]}{\left[{W_1}^2+(H_1-u)^2\right]}, & 0<u\le\Delta_1 \\ 2K_{\mathrm{s2}}\left[\sqrt{{H_2}^2+{W_2}^2}-\sqrt{\left(H_2-(u-\Delta_1+\delta)\right)^2+{W_2}^2}\right]\dfrac{[H_2-(u-\Delta_1+\delta)]}{\sqrt{\left(H_2-(u-\Delta_1+\delta)\right)^2+{W_2}^2}} & \\ +2W_2K_{\mathrm{r2}}\dfrac{\left[\alpha_2-\arctan\left(\dfrac{H_2-(u-\Delta_1+\delta)}{W_2}\right)\right]}{\left[{W_2}^2+[H_2-(u-\Delta_1+\delta)]^2\right]}+\dfrac{\partial T_{\mathrm{crs}}}{\partial u}. & \Delta_1<u\le 2H \end{cases} \tag{S7}$$

To ensure the continuity of the piecewise function F_{load}, δ is physically interpreted as the preload displacement to compensate for the initial value of the force F_{load} in the 2nd-stage deformation (otherwise F_{load} is 0 when u equals to Δ_1), which is determined by F_{load} at the time of making contact with CB ($u=\Delta$ in the 1st stage).

The equivalent widths W_1, W_2 and heights H_1, H_2 of the beam are determined by the unit cell size. W_1 is the total beam span, i.e., $W_1=15\times2+6=36$ mm (The width 6 mm refers to the loading platform width in the middle of the beam) and $H_1=12$ mm. According to the region of interest for CB, W_2 range from 15 mm to 25 mm ($W_2=W_1-2w$) and H_2 ranges from 3 mm to 10 mm. Moreover, K_{s1}, K_{s2} and K_{r1}, K_{r2} are respectively as:

$$K_{\mathrm{s}i}=\frac{EA}{2L_i},\ K_{\mathrm{r}i}=\chi(u)\frac{EI}{2L_i},\qquad i=1,2 \tag{S8}$$

where A and I are the beam cross-section area and moment of inertia of the cross-section. It is worth emphasizing that since there is a noticeable angular change in the beam during loading and considering the variations in the transition behaviors of beams with different coefficients g, we empirically introduce $\chi(u)$ to assist in adjusting the rotating spring stiffness at different displacements. The relationship that exists between the given parameters is:

$$
\begin{aligned}
A &= tb, \\
I &= \frac{t^3 b}{12}, \\
L_i^2 &= H_i^2 + W_i^2, \qquad i = 1, 2 \\
\alpha_i &= \arctan\left(\frac{H_i}{W_i}\right), \\
\Delta_1 &= 2H - 2H_2,
\end{aligned}
\tag{S9}
$$

where t and b are beam thickness and out-of-plane thickness.

The adjustment coefficient $\chi(u)$ of torsional spring stiffness is defined as:

$$
\chi(u) = \frac{(p_1 + p_2\alpha(u))}{\alpha(u) + q_1/Q(H_i, W_i)}, \qquad i = 1, 2 \tag{S10}
$$

where p_1, p_2, q_1 are constant factors, depending on the model size and material properties. In this work, for Beam 2 during loading, $p_1 = -250$, $p_2 = 800$, $q_1 = 0.44$. $\alpha(u)$ is the equivalent angular value, expressed as:

$$
\alpha(u) = \begin{cases} \arctan\left(\dfrac{H_1 - u}{W_1}\right), & 0 < u \le \Delta_1 \\ \arctan\left(\dfrac{H_2 - (u - \Delta_1)}{W_2}\right). & \Delta_1 < u \le 2H \end{cases} \tag{S11}
$$

The function $Q(H_i, W_i)$ is defined as:

$$
Q(H_i, W_i) = \frac{H_i}{W_i}\frac{W_r}{H_r}, \qquad i = 1, 2 \tag{S12}
$$

where W_r, H_r are the equivalent reference length and width of the beam, here we give $H_r = 7.5$, $W_r = 18$.

As a complementary term to the slip phenomenon, $\frac{\partial T_{crs}}{\partial u}$ is defined as:

$$
\frac{\partial T_{crs}}{\partial u} = \left[I(W_2 \le A) \times I\left(\frac{H_2}{2(W_1 - W_2)^2} \le B\right)\right] \xi(W_2, H_2) e^{-\frac{((u-\Delta) - 1.5W_2\tan\alpha_2)^2}{2W_2\tan\alpha_2}}, \tag{S13}
$$

where I(condition) is an indicator function, expressed as:

$$
I(\text{condition}) = \begin{cases} 1, & \text{condition is true} \\ 0. & \text{condition is false} \end{cases} \tag{S14}
$$

As analyzed in Section S4, with a fixed friction coefficient μ, slip occurs as the inclination γ decreases resulting in the coefficient $f_s < 1$. This condition is interpreted as W_2 is smaller than the coefficient A, meanwhile H_2 satisfies $\frac{H_2}{2(W_1 - W_2)^2}$ is smaller than the coefficient B.

In a uniaxial cyclic test of the unit cell, the energy cost (E_{out}) for the beam back to the initial state (reinitiation) can be reckoned as the inverse process of the 2nd-stage deformation during loading, the force (F_{unload})-displacement (u) relationship in this stage expressed as:

$$F_{\text{unload}} = \begin{aligned} &-Ratio[2W_2K_{r2}\frac{[\alpha_2-\arctan\left(\frac{H_2-(u-\Delta_1)}{W_2}\right)]}{\left[W_2{}^2+[H_2-(u-\Delta)]^2\right]} \\ &+2K_{s2}\left[\sqrt{H_2{}^2+W_2{}^2}-\sqrt{\left(H_2-(u-\Delta_1)\right)^2+W_2{}^2}\right]\frac{[H_2-(u-\Delta_1)]}{\sqrt{\left(H_2-(u-\Delta_1)\right)^2+W_2{}^2}}]. \end{aligned} \tag{S15}$$

The coefficients p_1, p_2, q_1 in K_{r2} are modified during unloading. Furthermore, the contrast between the clamping force caused by CB and the restoring force of the beam itself in the 2nd-stage deformation results in two different patterns (a wave peak or a wave trough) during unloading, distinguished by the black dotted line in Fig. S9.

Because of the difference caused by the two reinitiation modes, *Ratio* is introduced as the adjustment factor, defined as:

$$Ratio = \begin{cases} 1, & |F_{\text{trough}}| \le |F_{\text{boundary}}(W_2, H_2)| \\ \dfrac{F_{\text{boundary}}}{F_{\text{trough}}}, & |F_{\text{trough}}| > |F_{\text{boundary}}(W_2, H_2)| \end{cases} \tag{S16}$$

where $F_{\text{boundary}}(W_2, H_2)$ is the clamping force caused by the CB structure. When the absolute value of restoring force of the beam itself (F_{trough}) during unloading is smaller than F_{boundary}, the unloading pattern of the beam can be regarded as the inverse process of the loading period. Otherwise, a wave peak appears during unloading, and the transition behavior of the reinitiation is modified by the *Ratio*. From the energy cost for reinitiation (E_{out}) during unloading in Fig. S9, we can see the energy trapping is also several times higher than the classical cosine-shaped Beam 1 (E_{in}/WHb = 20 J/mm^3) at large w and small h.

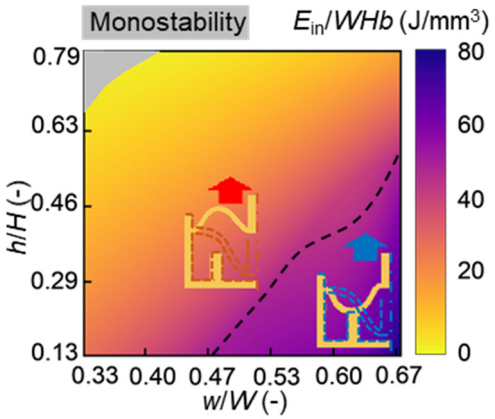

Fig. S10. Phase diagrams for the energy cost for reinitiation per volume E_{out}/WHb of the spring model in the parameter space of Single-CB position (w, h).

S6. Experimental results for Single-CB design

Fig. S11 shows the effect of w and h of Single-CB on the transition behaviors under a uniaxial cyclic test. From the stress-strain curves of different w in Fig. S11a-c, an increase of w leads to a greater F_{max} and a smaller F_{min} (negative value). Meanwhile, F_{max} and F_{min} each appear at almost the same strain. From the stress-strain curves of different h in Fig. S11d-f, we conclude that as h increases, F_{max} and F_{min} appear at greater strains with nearly the same force values. The proposed spring model provides a good explanation for these phenomena. As discussed in Fig. 2c, the equivalent stiffness, K_s and K_r, are positively correlated with w and $1/h$. Specifically, when the angle α_1 is small, K_s and K_r are dominantly affected by w. Thus, an increase in w significantly increases F_{max}, whereas an increase in h leads to a nearly constant F_{max}. Besides, although w changes, the equivalent height H_2 of the beam stays the same, F_{max} appears in the same displacement process. This also explains that F_{max} appears in a larger strain with an increase of h, i.e., the equivalent height H_2 decreases.

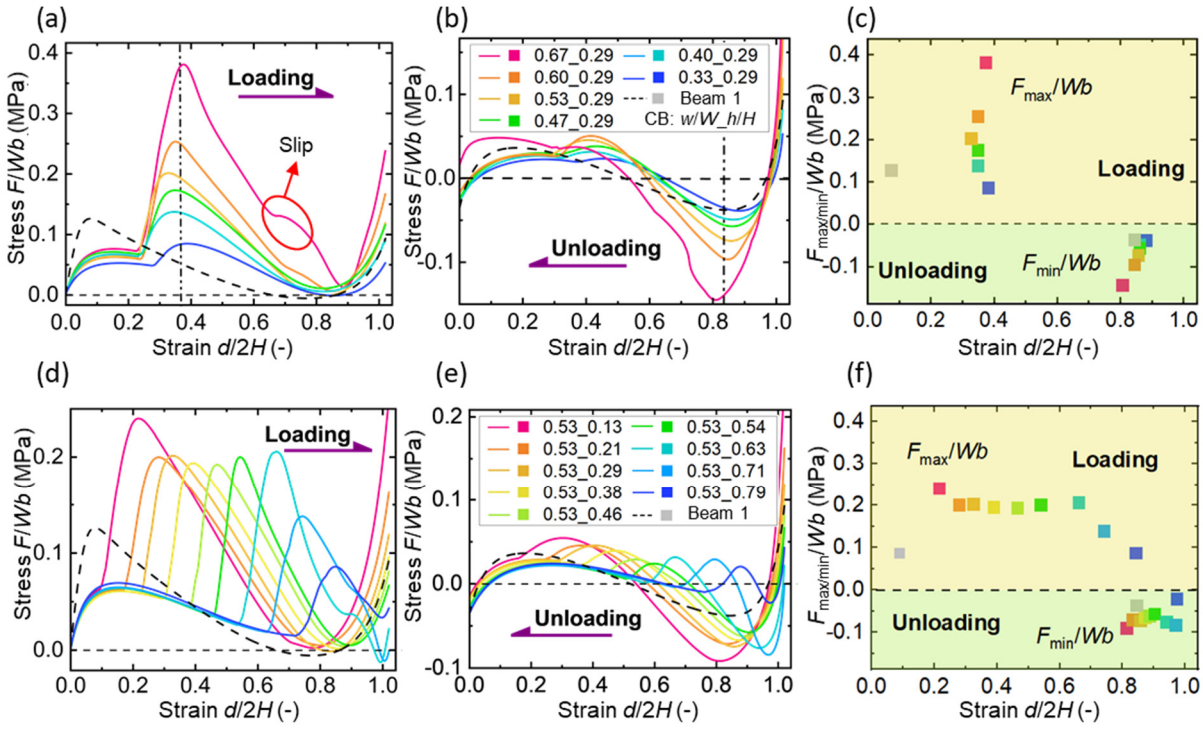

Fig. S11. Effect of Single-CB position (w, h) on the transition behaviors studied by experiments. (a) and (b) Stress-strain curves of Single-CB with different w/W during loading and unloading respectively (at fixed h/H: 0.29). (c) The snapping force per area F_{max}/Wb and the trough force per area F_{min}/Wb during loading and unloading. (d) and (e) Stress-strain curves of Single-CB with different h/H during loading and unloading respectively (at fixed w/W: 0.53). (f) The

snapping force per area F_{max}/Wb and the trough force per area F_{min}/Wb during loading and unloading.

S7. Spring model and experimental results for Multi-CB (n = 2) design

The spring model for Multi-CB is decoupled into multiple Single-CB conditions, and the beam transitions to the subsequent deformation stage upon making contact with each new CB. It is worth emphasizing that the deformation state of the beam after making contact with the preceding CB(s) informs the subsequent CB design. When n = 2, the deformation process undergoes three distinct stages. While the initial two stages align with the Single-CB scenario, the 3rd-stage deformation, subsequent to contacting the 2nd CB, is influenced by the deformation pattern that follows the contact with the 1st CB.

As illustrated in Video S3, the 1st-stage and the 2nd-stage deformation for Multi-CB with n = 2 (1st CB: 0.33_0.13, 2nd CB: 0.67_0.38) are consistent with the Single-CB (CB: 0.33_0.13). The initial deformation state in the 3rd-stage deformation for Multi-CB is the intermediate deformation state of the 2nd-stage deformation for the Single-CB case (CB: 0.67_0.38), shown in Fig. S11. This difference is reflected by a displacement difference Δu in the spring model. Additionally, the initial angle α_3 is smaller, while the equivalent compression and rotation stiffness remain the same ($K_{s3} = K_{s2}$, $K_{r3} = K_{r2}$ in Fig. S12). Δu is related to both the 1st CB position and the 2nd CB position, i.e.:

$$\Delta u = f(h, w, h', w'). \tag{S17}$$

In our study, we investigate the effect of the 2nd CB position of Multi-CB on the transition behaviors through a fixed 1st CB: 0.33_0.13. Δu is expressed as:

$$\Delta u = \sum_{i=0}^{3} \sum_{j=0}^{3} a_{ij} h'^{i} w'^{j}. \tag{S18}$$

The influence of the coupling between CBs on the transition behavior is quantified by Δu. Consequently, the force (F_{load})-displacement (u) relationship for the 3rd-stage deformation ($\Delta_2 < u \leq 2H$) are:

$$F_{\text{load}} = \begin{aligned} &2K_{s3}\left[\sqrt{H_3^2+W_3^2}-\sqrt{\left(H_3-(u+\Delta u-\Delta_2+\delta)\right)^2+W_3^2}\right]\frac{[H_3-(u+\Delta u-\Delta_2+\delta)]}{\sqrt{\left(H_3-(u+\Delta u-\Delta_2+\delta)\right)^2+W_3^2}} \\ &+2W_3K_{r3}\frac{[\alpha_3-\arctan\left(\frac{H_3-(u+\Delta u-\Delta_2+\delta)}{W_3}\right)]}{\left[W_3^2+[H_3-(u+\Delta u-\Delta_2+\delta)]^2\right]}, \end{aligned} \tag{S19}$$

where H_3, W_3, K_{s3}, K_{r3} can be obtained through the Single-CB case (CB positioned at the 2nd CB position of Multi-CB).

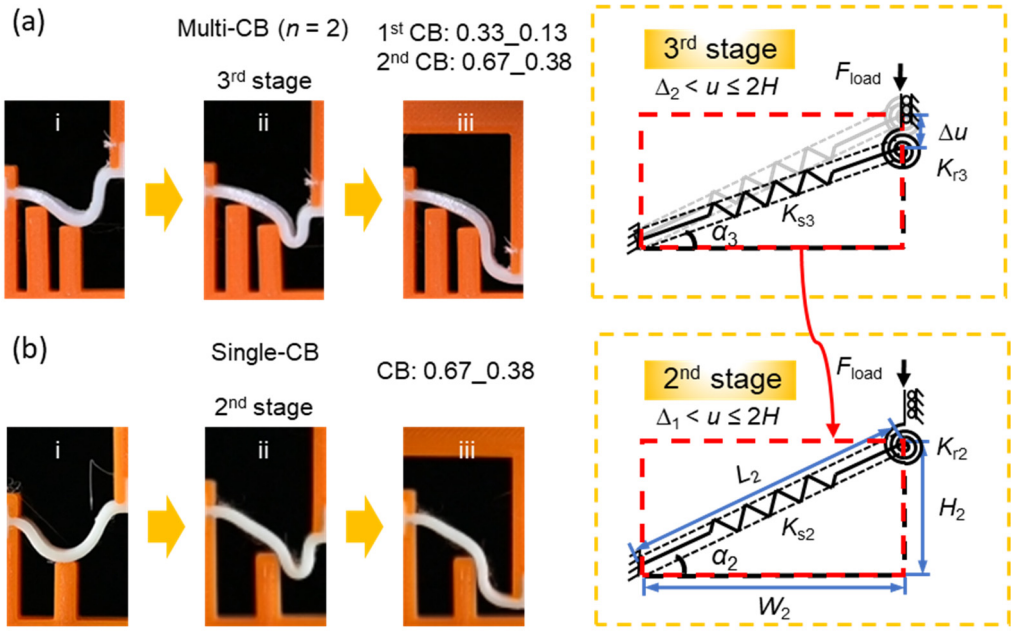

Fig. S12. Comparison of spring model and deformation patterns for (a) Multi-CB (n = 2) case and (b) Single-CB case.

Depending on the 2nd CB position, the transition behaviors manifest in two distinct cases, as illustrated in Fig. S13. Specifically, in the case of the 2nd CB positioned at 0.53_0.54, the snapping force per area F_{max}/Wb appears in the 2nd-stage deformation, which is determined by the 1st CB position. Conversely, when the beam makes contact with the 2nd CB positioned at 0.53_0.21, the snapping force per area F_{max}/Wb appears in the 3rd-stage deformation (after contacting the 2nd CB) and it is further modulated by the 2nd CB position. This case exhibits multiplateau behavior, which is expected to develop hierarchical mechanical performances.

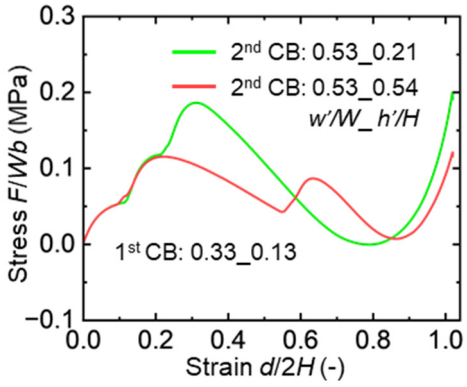

Fig. S13. The stress-strain curves of the 2nd CB positioned at 0.53_0.21 and 0.53_0.54. The snapping force per area F_{max}/Wb occurs in the 3rd-stage deformation for the former, exhibiting multipateau behavior.

S8. Spring model and experimental results for Sloped-CB design

As shown in Fig. S14, the spring model for Sloped-CB is divided into three stages. Compared to Single-CB case, an additional 2nd-stage deformation is introduced, in which the fulcrum on CB for beam deformation is adjusted. We need to clarify that this stage is partially present under Single-CB conditions, as exemplified in Case 2 of the slip phenomenon in Section S4. In this scenario, the contact point between Beam 2 and CB is on the CB platform and the subsequent 2nd-stage deformation of the beam conducts upon the top-right vertex of CB, which means the fulcrum is adjusted. Nevertheless, given the rapid transformation of this stage in Single-CB conditions, its inclusion in Single-CB analysis is considered unnecessary. Conversely, this stage exerts a notable influence on the transition behavior in Sloped-CB conditions.

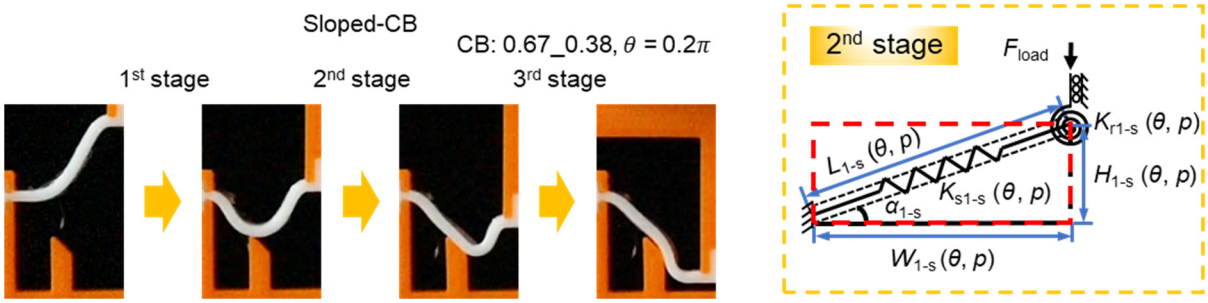

Fig. S14. Spring model and deformation patterns for Sloped-CB case.

The deformation pattern of the beam in contact with CB is influenced by the position of CB, as well as the inclination and width of Sloped-CB. The force (F_{load})-displacement (u) relationship at this stage can be expressed as:

$$F_{\text{load}} = g(h, w, \theta, p, u). \tag{S20}$$

Within the spring model, we simplify the fulcrum adjustment, i.e., the 2nd-stage deformation by treating it as a deformation stage based on a fixed equivalent fulcrum. Thus, compared to Equation (S7), the force (F_{load})-displacement (u) relationship after making contact with CB ($\Delta_1 < u \leq 2H$) modifies as:

$$F_{\text{load}} = \begin{cases} 2K_{\text{s1-s}}\left[\sqrt{{H_{\text{1-s}}}^2+{W_{\text{1-s}}}^2}-\sqrt{\left(H_{\text{1-s}}-(u-\Delta_1+\delta)\right)^2+{W_{\text{1-s}}}^2}\right]\dfrac{[H_{\text{1-s}}-(u-\Delta_1+\delta)]}{\sqrt{\left(H_{\text{1-s}}-(u-\Delta_1+\delta)\right)^2+{W_{\text{1-s}}}^2}} \\ +2W_{\text{1-s}}K_{\text{r1-s}}\dfrac{[\alpha_2-\arctan\left(\frac{H_{\text{1-s}}-(u-\Delta_1+\delta)}{W_{\text{1-s}}}\right)]}{\left[{W_{\text{1-s}}}^2+[H_{\text{1-s}}-(u-\Delta_1+\delta)]^2\right]}, & \Delta_1 < u \leq \Delta_{\text{1-s}} \\ 2K_{\text{s2}}\left[\sqrt{{H_2}^2+{W_2}^2}-\sqrt{\left(H_2-\left(u-\Delta_{\text{1-s}}+\delta^{'}\right)\right)^2+{W_2}^2}\right]\dfrac{\left[H_2-\left(u-\Delta_{\text{1-s}}+\delta^{'}\right)\right]}{\sqrt{\left(H_2-\left(u-\Delta_{\text{1-s}}+\delta^{'}\right)\right)^2+{W_2}^2}} \\ +2W_2K_{\text{r2}}\dfrac{[\alpha_2-\arctan\left(\frac{H_2-\left(u-\Delta_{\text{1-s}}+\delta^{'}\right)}{W_2}\right)]}{\left[{W_2}^2+\left[H_2-\left(u-\Delta_{\text{1-s}}+\delta^{'}\right)\right]^2\right]}, & \Delta_{\text{1-s}} < u \leq 2H \end{cases} \tag{S21}$$

where $\Delta_{\text{1-s}}$ is the displacement at the end of the fulcrum adjustment stage.

In our study, we investigated the effect of the inclination θ and the width p of Sloped-CB on the transition behaviors through several fixed CB positions. As shown in Fig.s 2f,g, the fixed CB position is 0.33_0.13 ($\theta = 0$), an increase in θ for CB correlates with a reduction in stiffness k_{s} and F_{max} after making contact with CB. The equivalent width $W_{\text{1-s}}$ and height $H_{\text{1-s}}$ in the 2nd-stage deformation are defined as:

$$W_{\text{1-s}} = 32+2p(\sin(\theta)-1), \tag{S22}$$

$$H_{\text{1-s}} = 10-\frac{p}{2}\tan(\theta). \tag{S23}$$

$W_{\text{1-s}}$ is positively correlated with $1/p$ and $\sin(\theta)$, and when θ is small, the change of p has a more significant influence on $W_{\text{1-s}}$. The coefficient $\chi^{'}(u)$ to assist in adjusting the rotating spring stiffness $K_{\text{r1-s}}$ are determined by:

$$\chi^{'}(u) = k\sin(a_1\theta+a_2)\sin(b_1\alpha(u-\Delta_1)+b_2). \tag{S24}$$

With an increase in θ, the impact of contact constraints imposed by CB on the transition behavior becomes progressively weak, as evidenced in Video S4 and Fig. S15, consistent with an increase in $W_{\text{1-s}}$ during the 2nd-stage deformation.

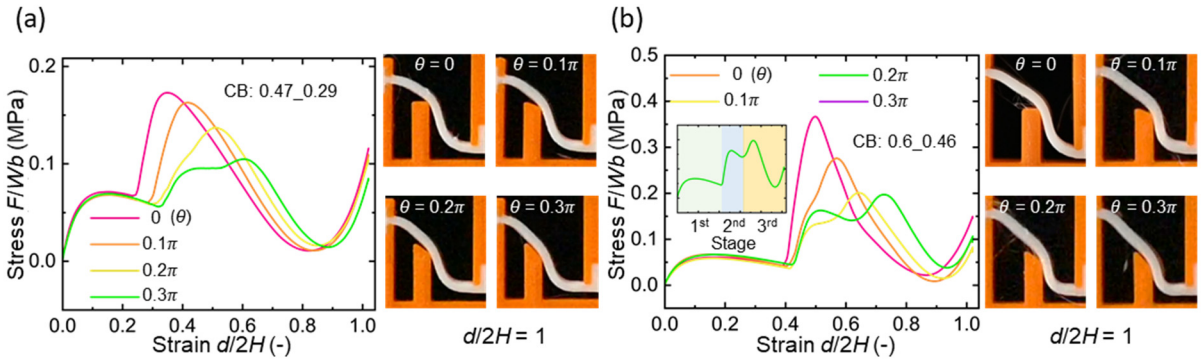

Fig. S15. Effect of CB shape at different positions on the transition behavior. (a) CB: 0.47_0.29. (b) CB: 0.6_0.46.

S9. Deformation patterns and transition behaviors of 2D array multistable metamaterials

Compared with the snapping forces controlled by the thickness of the classical metamaterial, the assembled metamaterial tunes snapping forces by CB units. Because of the CB effect, a quasi-zero stiffness zone occurs in the transition behaviors shown in Fig. S16a. The transition behaviors of the unit cells that make up the assembled metamaterial are shown in Fig. S16b. Theoretically, the upper boundary F_u is $3F_{rm}$ (F_{rm} is the maximum force for unit cell in 1st-stage deformation), while the lower boundary F_l is $3\min\{F_{r1}, F_{r2}, F_{r3}\}$ (F_{r1}, F_{r2}, and F_{r3} are forces for three rows of unit cell contacting CB respectively). Due to the smooth transition behavior of Beam 2 in the early deformation stage, F_u and F_l are numerically close, which results in the quasi-zero stiffness zone. The length of this zone denoted as d_z, can be approximately considered as the cumulative displacement of three rows of unit cells that come into contact with CB. When starting from different initial states, such as State 2-II and 2-III, the assembled metamaterial exhibits the quasi-zero stiffness zone of different lengths, as shown in Fig. S17.

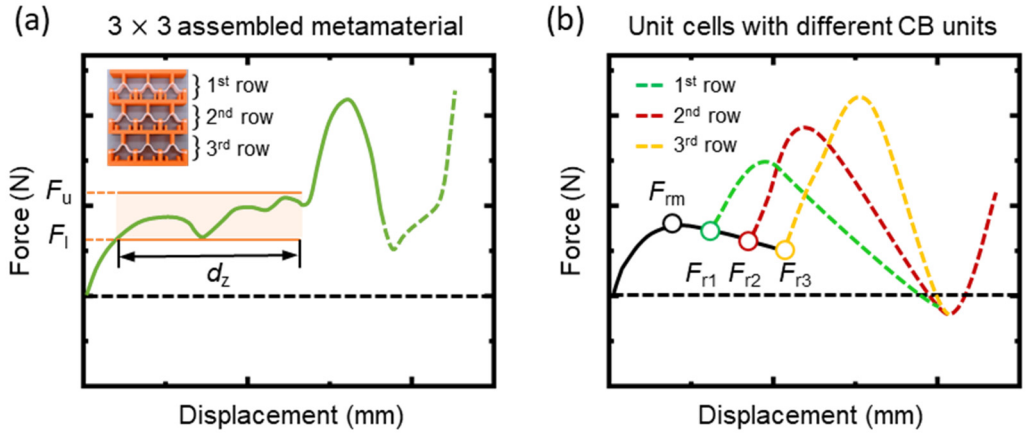

Fig. S16. The transition behaviors of (a) the assembled metamaterial and (b) the unit cells constituting the assembled metamaterial.

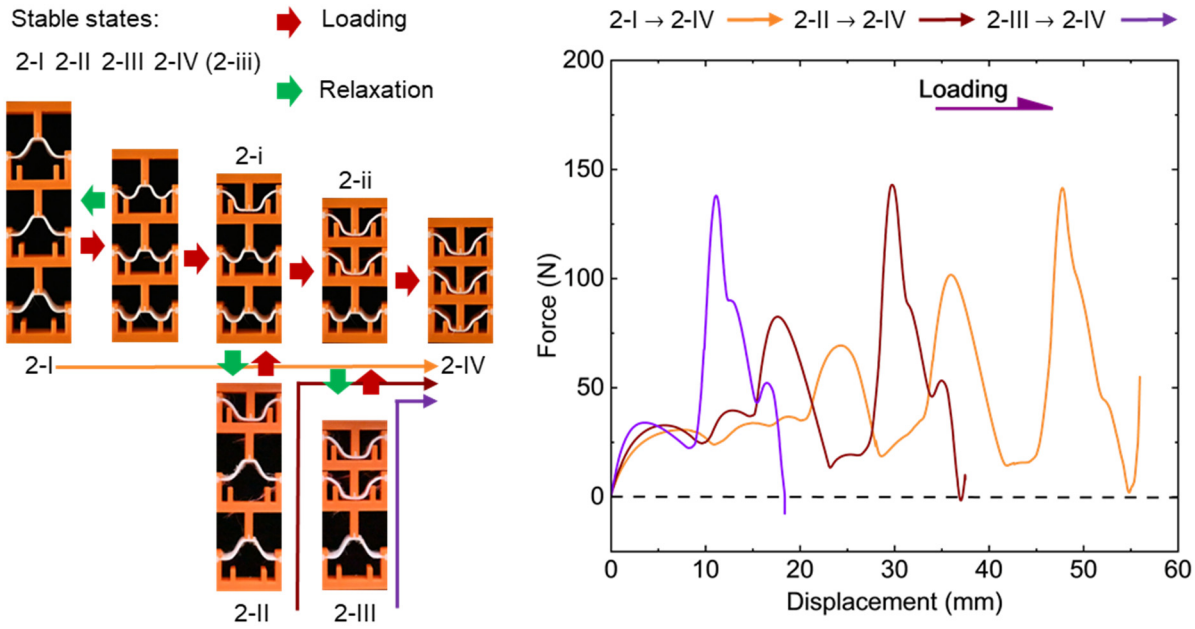

Fig. S17. Deformation configurations and transition behaviors of different stable-state transitions during loading.

As shown in Fig. S18, the assembled metamaterial exhibits consistent deformation configurations with the classical metamaterial during unloading. Meanwhile, the trough forces F_{min} are smaller than the classical ones from the force-displacement curves, indicating the stability of the stable states is improved via the locking effect of CB.

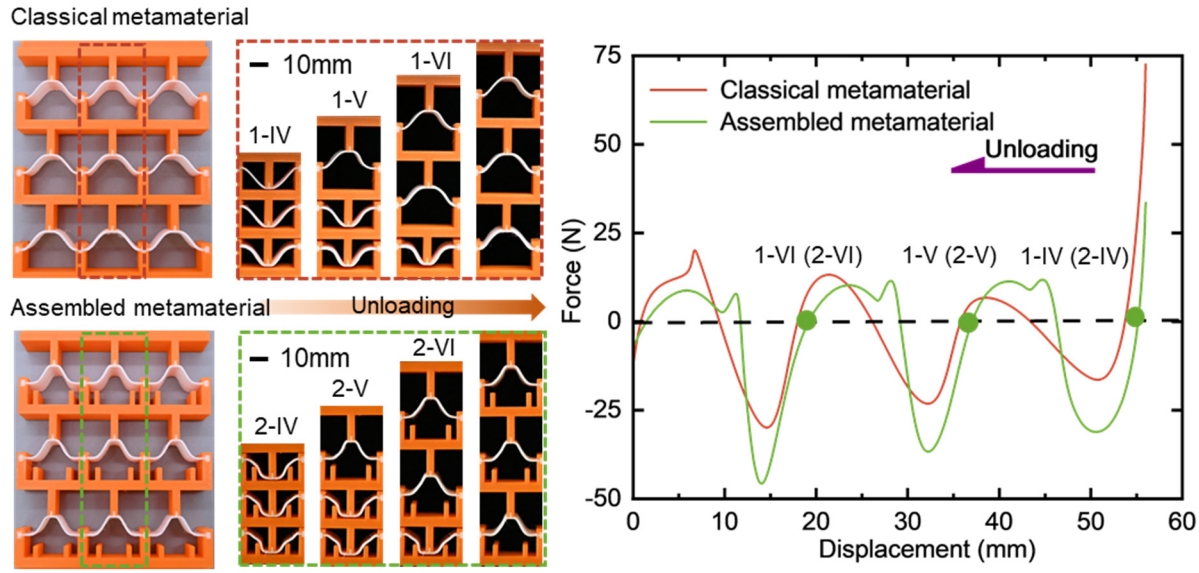

Fig. S18. Experimental deformation configurations and force-displacement curves for assembled metamaterial and classical metamaterial during unloading.

S10. Programmable multistability of the 3D unit cell

The multistable properties of 3D unit cells are mainly investigated by two strategies: the presence or absence of CB (with a fixed position: 0.53_0.54) and the use of either an unperforated or perforated shell[8]. The shell is obtained by rotating the 2D beam 360 degrees around the central axis. Additionally, we also compared the shells derived from the beams with different values of g, i.e., $g = 2$ (Beam 2) and $g = 1$ (Beam 1) in Fig. S19.

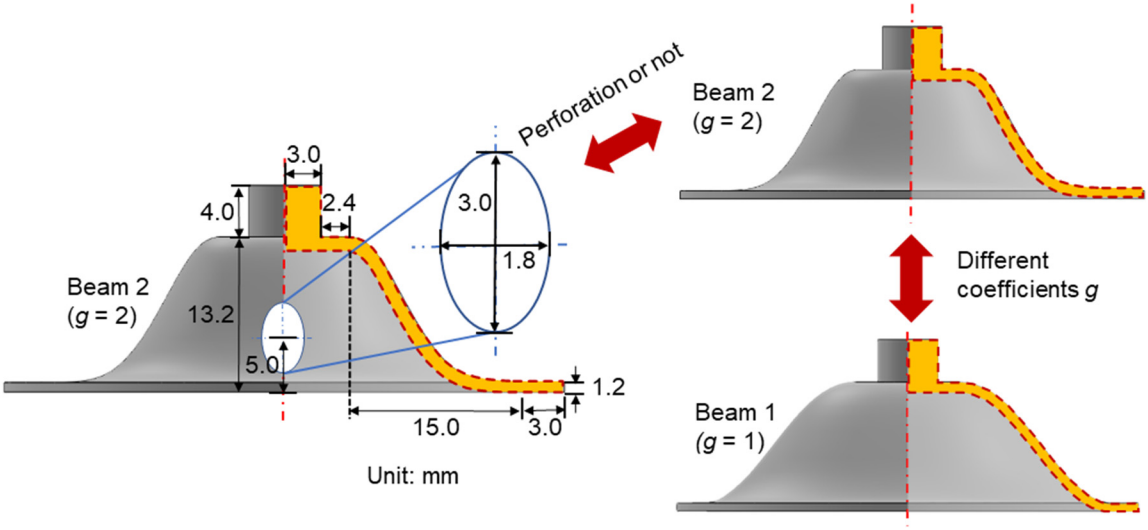

Fig. S19. Design strategies and details of the 3D shell to investigate multistable properties.

We observed that the shell derived from Beam 1 only exhibits bistability. Similar to the 2D beam case, since the shell stiffness at the loading end is smaller than that at the fixed end, the loading end of the shell first deforms, leading to a configuration exhibiting central concave and peripheral convexity in the intermediate deformation process. This pattern does not result in structural local discontinuity, i.e., it does not introduce another stable state (Fig. S20). Additionally, the perforated shell design only reduces the force values and also does not introduce a new stable configuration.

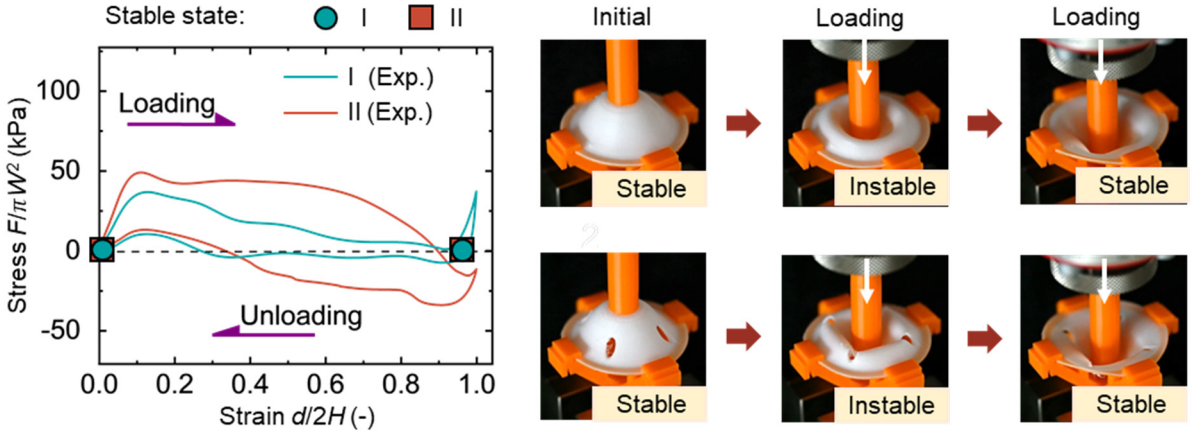

Fig. S20. Transition behaviors and deformation states of the perforated/unperforated shell with Beam 1.

Numerical simulation was conducted to visualize the transition behavior of the 3D unit cells, facilitating the CB design. The discretized mesh model is shown in Fig. S21. Because of the symmetric characteristics of the unit cell, to save computational time cost, 1/4 of the unit cell was used in the simulation.

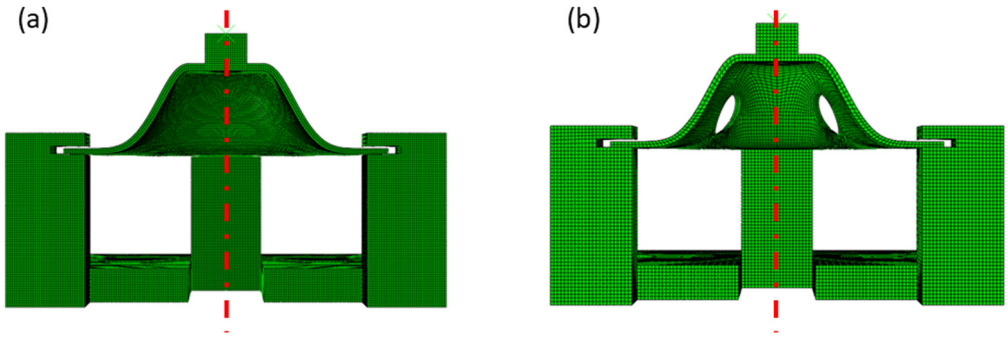

Fig. S21. The discretized mesh model of half of 3D unit cells. (a) The unperforated shell. (b) The perforated shell.

The shell derived from Beam 2 increases the stable state number to three by introducing an intermediate stable state. This can be found in Sample III in Fig. 4b, besides the initial state, two stable states were observed at strain around 0.7 and 1 during loading (Fig. S22). The intermediate stable state, i.e., State 2 or State 4 of Sample III shown in Fig. 4d, can be attributed to two contributing factors. On the one hand, compared to the shell derived from Beam 1, the shell derived from Beam 2 exhibits a different shell curvature of the shell, leading to the shell stiffness at the loading end being much larger than that at the fixed end. This drastic change in

stiffness and curvature of the shell is more likely to exhibit structural local discontinuity of the shell (central convexity and peripheral concave) during a cyclic test. On the other hand, the shell is printed layer by layer, and the bonding strength between layers is relatively weak, tending to be self-locked through structural discontinuities. This intermediate stable state occurs when the force value is positive from the stress-strain curves. The overall deformation states of the numerical simulation during loading are consistent with the experiment. However, as the material properties employed in the simulation do not account for the influence of the material printing process, and in order to enhance computational convergence, the local discontinuity is mitigated, thus intermediate stable states are not observed in the simulation.

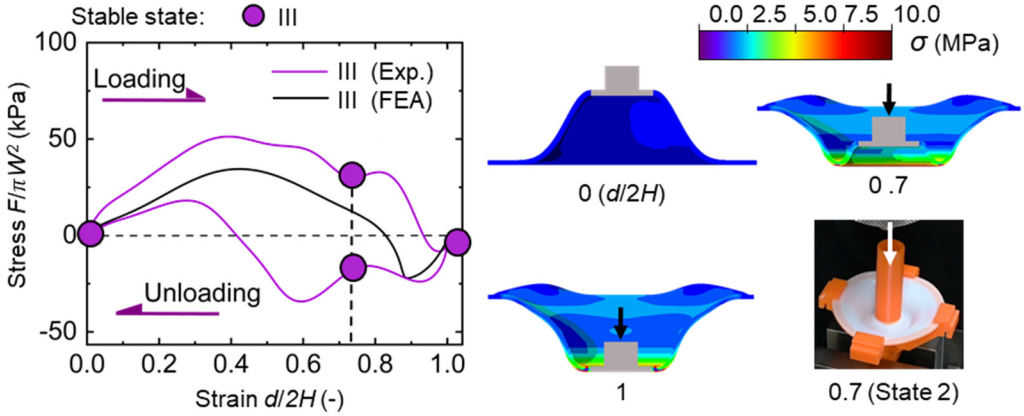

Fig. S22. Deformation patterns and stress-strain curves for experiments and numerical simulation of the unperforated shell.

The perforation strategy weakens the shell stiffness, resulting in a reduced force value (Fig. S23). In addition, a different deformation pattern caused by the perforation strategy further increases the stable state number to four, i.e., an additional intermediate stable motif (State 4 of Sample IV in Fig. 4d) appears at strain around 0.2 during unloading. This is because the position of the holes in the shell results in a more pronounced reduction of the shell stiffness at the fixed end than that at the loading end. Thus a diverse deformation pattern during unloading is introduced (the fixed end of the shell deforms first during unloading, while the loading end of the unperforated shell deforms first during unloading in Video S6, Supporting Information), leading to another structural self-locked state.

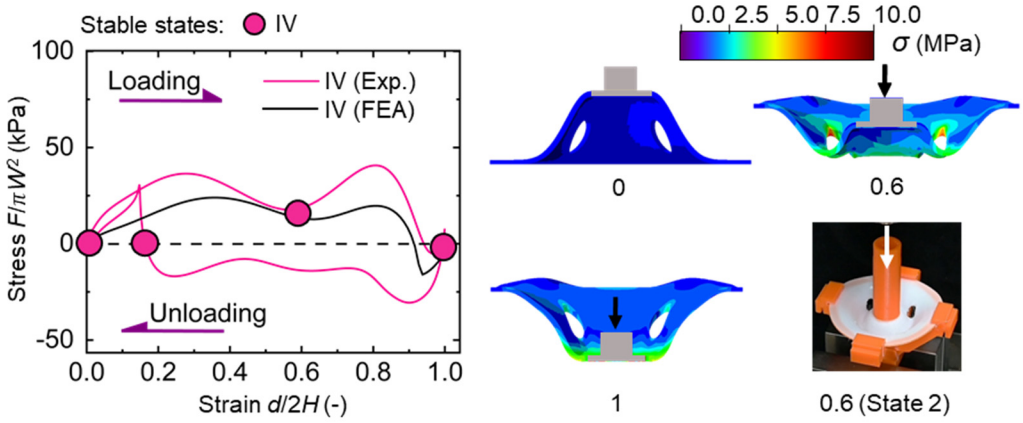

Fig. S23. Deformation patterns and stress-strain curves for experiments and numerical simulation of the perforated shell.

S11. The design of unit cells with customized multiplateau behaviors

Based on the progressive design process in Fig. 4, we obtained Integrated-CB-1 for the multiplateau behavior. By modifying the geometrical parameters, we can further yield customized multiplateau behavior via Integrated-CB, e.g., a smaller stress increment h_1 showing a better low-load protection characteristic via Integrated-CB-2. A comparison of the design steps of Integrated-CB-1 and Integrated-CB-2 is shown in Fig. S24. In Step 1, Integrated-CB-2 shares the same starting point as Integrated-CB-1. While Integrated-CB-2 with a smaller width p_1 leads to a smaller stress increment h_1. In the subsequent design steps, based on the new geometrical parameter p_1, Integrated-CB-2 is obtained by following the multiplateau design process. The specific parameters of both Integrated-CBs are illustrated in Fig. S24. Integrated-CB-2 shows quite different geometrical parameters from Integrated-CB-1, corroborating the correlation of each step of CB design.

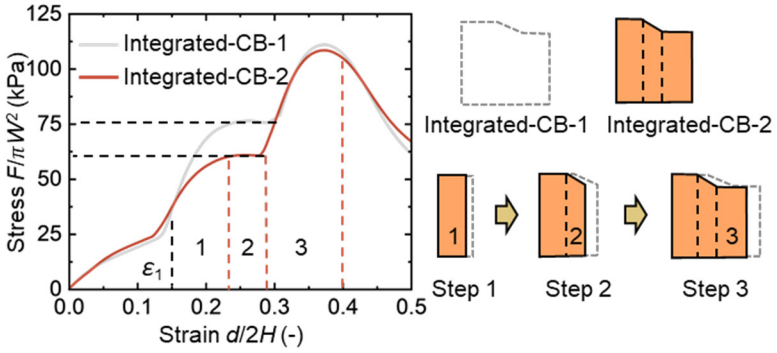

$(w, h) = (3.0, 2.2)$ Unit: mm

Parameters	p_1	θ_2	p_2	p_3
Integrated-BC-1	3.0	$\frac{\pi}{6}$	3.0	3.0
Integrated-BC-2	2.5	$\frac{\pi}{5}$	2.4	3.5

Fig. S24. A comparison of the progressive CB design details of customized multiplateau behaviors.

S12. The design of unit cells with linear stiffness and quasi-zero stiffness behaviors

As shown in Fig. S25, the primary descriptors for modulating linear stiffness behavior involve maintaining consistent stiffness within three local intervals, thereby ensuring uniform slopes across the modulation range. Thus we adopt the design strategy of three Sloped-CBs combinations. The starting point (w, h) also positions at the bottom point of the shell when the strain is ε_1, which is the same as the modulation of multiplateau behavior. In Step 1, the local stiffness within interval 1 is modulated to k by the inclination θ_1 and further the width p_1 of CB 1 modulates the interval length L_1. Similarly, in Steps 2 and 3, based on the inclinations θ_2 and θ_3 tunes the local stiffness, the widths L_2 and L_3 modulate the length of Intervals 2 and 3. The specific parameters of the designed Interated-CB are illustrated in Fig. S25.

Here, it is imperative to note that an upper limit exists for the length of Intervals 1-3, which collectively constitute the modulation region. This limitation arises due to the influence of Sloped-CB inclination on the modulation of local stiffness, affecting only a constrained range of intervals. For example, the transition behavior induced by CB designed in Step 2 does not maintain a linear stiffness in Interval 3. Subsequently, this interval undergoes further modulation by the designed Sloped-CB 3 in Step 3. We conclude that a one-step Sloped-CB design demonstrates the capability to encompass a modulation interval of 0.1 strain length. Consequently, the integration of three Sloped-CBs effectively fulfills the modulation requirements, achieving an upper strain limit of 0.45. More precise modulation can also be achieved by dividing modulation interval into more subintervals, i.e., by using more combinations of Sloped-CBs.

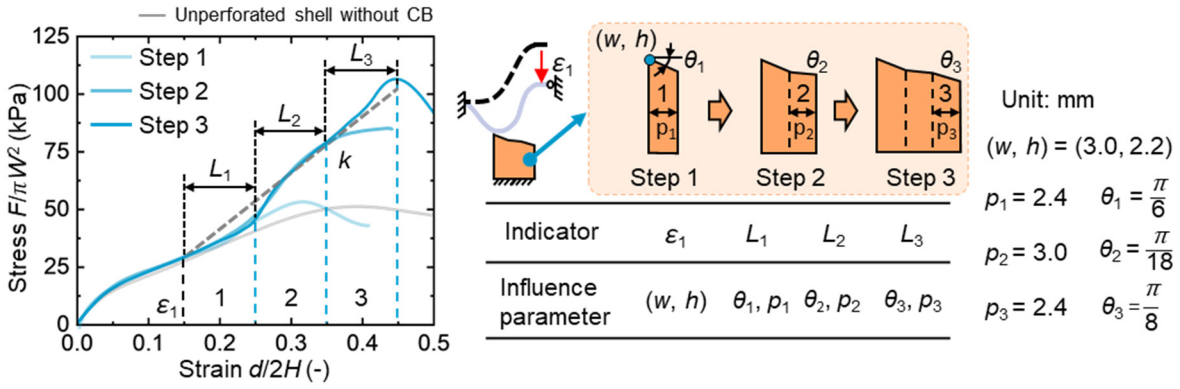

Fig. S25. The progressive CB design details and experimental stress-strain curves of linear stiffness behavior.

The quasi-zero stiffness behavior is expected to exhibit vibration isolation at diverse force values. Thereby, the primary descriptors include the force value and local stiffness modulation. The corresponding design strategy is the perforation strategy and Sloped-CBs combination in Fig. S26. With the perforation strategy, the force value reduces while the deformation patterns of the shell also change. Through the transition behavior of a perforated shell without CB, we determine the initial strain ε_1' and the modulation of the quasi-zero stiffness is achieved by a two-step design. In addition to the quasi-zero stiffness exhibited by the collective interaction of arrayed unit cells in Section S9, here it is obtained through the beam-CB contact.

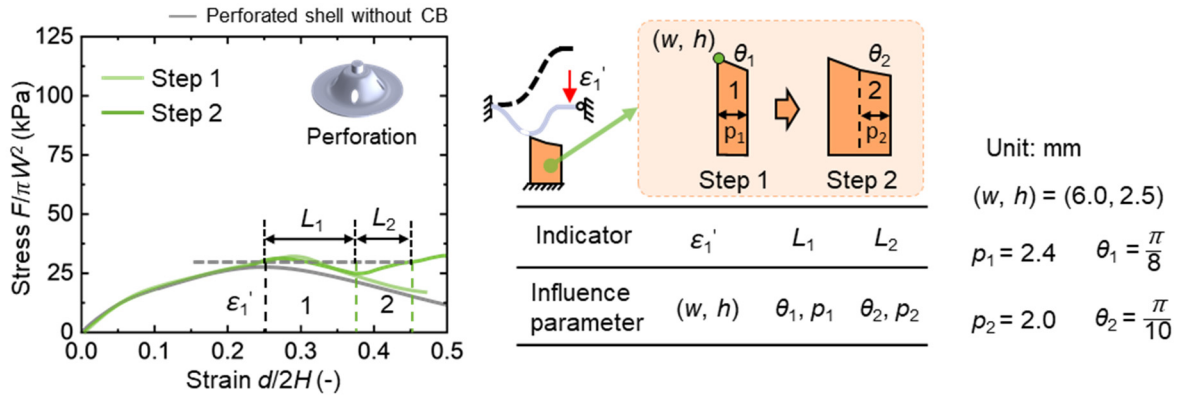

Fig. S26. The progressive CB design details and experimental stress-strain curves of quasi-zero stiffness behavior.

S13. Experimental details of plate-type digital materials with rapid reconfigurability for various application scenarios

Based on the modulated function-oriented transition behaviors, i.e., multiplateau behavior, linear stiffness, and quasi-zero stiffness, we further employed an in-plane array of prescribed unit cells to construct plate-type digital materials in Fig. S27. The assembled metamaterial consisted of an array of 8 unit cells, distinguished by the feature of replaceable shells and CB plates. In our experimental setup, we incorporated four perforated shells and four unperforated shells. Through the substitution of the designed CB plates, the transition behavior of the digital material could swiftly transition from a tailored multiplateau to linear stiffness, enabling rapid adaptation to a variety of application scenarios. Moreover, multistability (snap-through behavior) endows digital materials with self-protective properties in the face of an overloading situation.

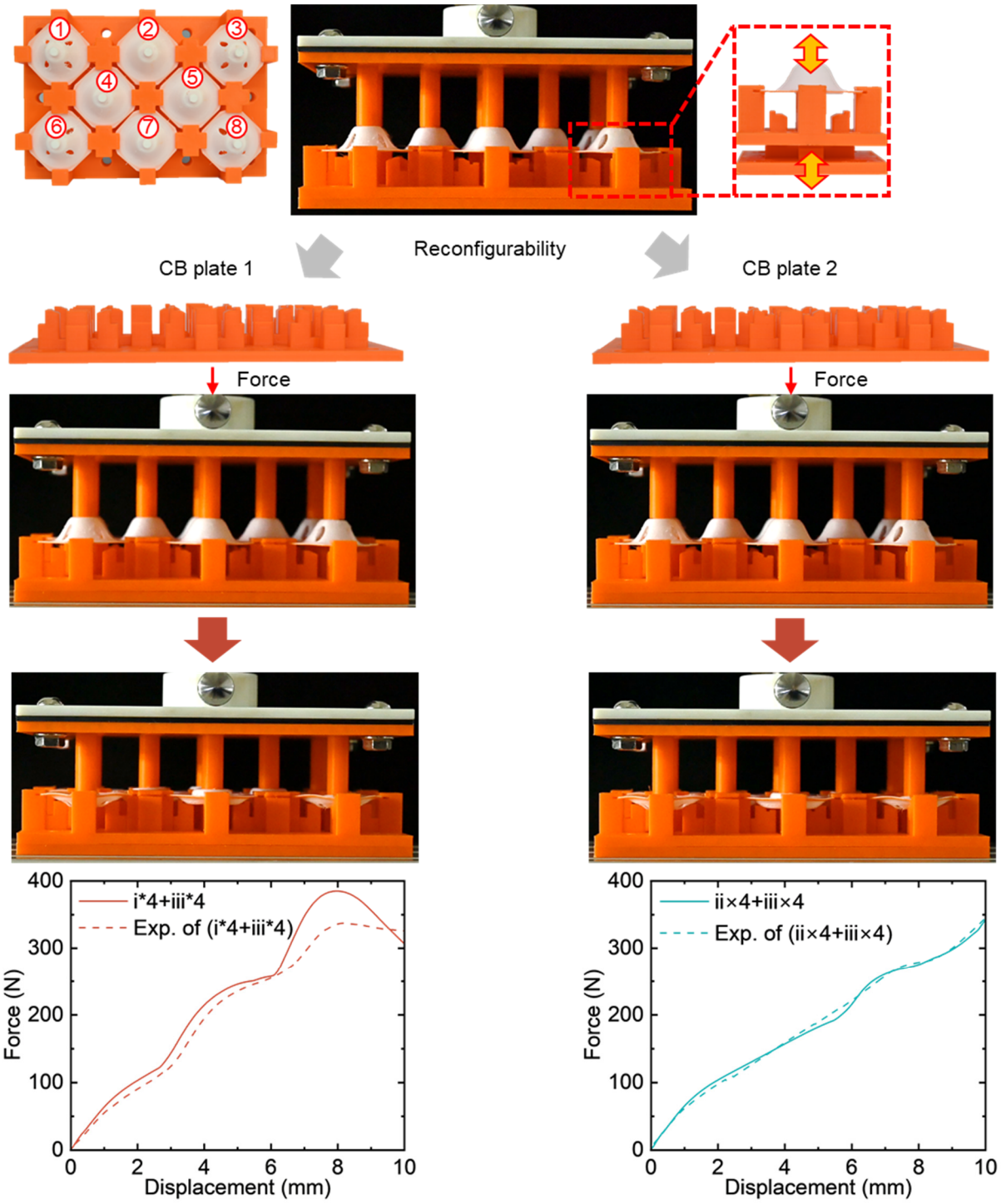

Fig. S27. Plate-type digital materials with rapid reconfigurability to accommodate different application scenarios via the replacement of CB plates.

Reference

[1] J. Qiu, J. H. Lang, A. H. Slocum, *J. Microelectromechanical Syst.*, 2004, **13**, 137.

[2] H. Yang, L. Ma, *Mater. Des.*, 2020, **188**, 108430.

[3] H. Darijani, R. Naghdabadi, *Acta Mech.*, 2010, **213**, 235.

[4] M. T. Shaw, W. J. MacKnight, *Introduction to polymer viscoelasticity*, John Wiley & Sons, **2018**.

[5] R. Elleuch, K. Elleuch, H. Ben Abdelounis, H. Zahouani, *Mater. Sci. Eng. A*, 2007, **465**, 8.

[6] D. P. Holmes, *Curr. Opin. Colloid Interface Sci.*, 2019, **40,** 118.

[7] T. Chen, J. Panetta, M. Schnaubelt, M. Pauly, *ACM Trans. Graph.*, 2021, **40**, 39.

[8] J. Shi, H. Mofatteh, A. Mirabolghasemi, G. Desharnais, A. Akbarzadeh, *Adv. Mater.*, 2021, **33**, 2102423.